

Flow state in molecular-dynamics-simulated deformed amorphous Ni_{0.5}Zr_{0.5}

K. Brinkmann* and H. Teichler

Institut für Materialphysik und Sonderforschungsbereich 602, Universität Göttingen, Hospitalstrasse 3/7, 37073 Göttingen, Germany

(Received 21 June 2002; published 15 November 2002)

Results are reported from molecular dynamics simulations about the deformation behavior of amorphous metallic Ni_{0.5}Zr_{0.5} alloys near their glass transition temperature. Constant shear strain rate and constant shear stress deformations are analyzed. Stress-strain curves from constant shear strain rate deformations reveal different stages of deformation, first a regime with approximately linear stress-strain relation, then a transient regime with pronounced strain softening, and finally, for large strains, a nearly strain-independent flow stress region. The strong stress overshoot in the transient regime is ascribed to a delayed transition under steady-state deformations from the initial glassy state into a structurally and dynamically different one. This flow state shows a decreased viscosity, an increased potential energy per atom, and a loss of short-range order, the latter being deduced from the radial distribution functions. In the flow state, the self-part of the intermediate scattering function reveals an unchanged vibration spectrum of the system but a faster decay of density correlations compared to the starting structure. Creep curves from constant shear stress deformations show a nearly linearly increasing strain for moderate shear stresses and moderate deformations. The strain rate depends in a non-Newtonian manner on stress with an activation volume of $7-8 \times 10^{-29} \text{ m}^3$. Deformation simulation with large constant shear stress leads to an instability, identified as the transition into the flow state.

DOI: 10.1103/PhysRevB.66.184205

PACS number(s): 81.05.Kf, 52.65.Yy, 81.40.Lm, 83.60.Rs

I. INTRODUCTION

The present contribution reports results from molecular dynamics (MD) investigations of a model metallic glass subjected to shear deformations. External mechanical deformations provide an alternative tool to probe the dynamical properties of the glassy state in addition to the more common methods like neutron- or light-scattering, dielectric spectroscopy, or tracer diffusion measurements. Mechanical deformations have been carried out at constant rate, for example, by Kawamura *et al.*¹ as tensile deformations, by Kato *et al.*² as compression tests, or as creep experiments (see, e.g., Mad-din and Masumoto,³ Taub,⁴ Stromböm *et al.*,⁵ Weiss *et al.*⁶ or Ocelik *et al.*⁷).

Here we report results from MD simulations of pure shear deformations for a computer model adapted to the binary intermetallic compound Ni_{0.5}Zr_{0.5}. The processes studied are close to the experimental situations investigated by, e.g., Kato *et al.*² for the constant-strain-rate case and Weiss *et al.*⁶ for the constant-stress case. The Ni_{0.5}Zr_{0.5} system was chosen because it is a glass-forming alloy investigated well in MD simulations (see, e.g., Teichler⁸ and the references therein), indicating qualitative as well as quantitative conformity (cf. Teichler⁹) to experiments¹⁰⁻¹³ and because its elements are important components of some of the recently discovered massive glass-forming metallic systems.¹⁴ Mechanical deformation studies are aimed at contributing results on the low-frequency dynamics of glasses, complementary to the high-frequency data available, for example, from spin-echo measurements.¹⁵⁻¹⁷

Regarding the research on metallic glasses in the past, it should be mentioned that attempts have been made to understand the mechanical behavior of the glasses not only from the experimental and computational side but also from theoretical calculations based on microscopic pictures describing the reorientations of atoms under shear. Here the reader is

especially referred to the early work of Spaepen,¹⁸ who describes the deformation as arising from diffusional single-atom jumps biased by an external load, or the investigations of Argon,¹⁹ where, briefly summarized, the plastic response is viewed to be due to reorientations of atomic clusters containing a number of atoms, and also the work of Tomida and Egami,²⁰ who developed the bond-exchange mechanism.

Beyond the scope of the above-mentioned investigations the question remains whether there exist state variables for the glassy system that determine the state of the system and hence a possibly varying response to external deformations. A promising first approach regarding this was provided by Falk and Langer.²¹ They investigated the response of a two-dimensional Lennard-Jones glass exposed to an external shear stress by introducing the density of shear transformation zones as an additional state quantity. We should quote here also the Monte Carlo (MC) simulations for a Lennard-Jones model by Utz *et al.*²² When subjecting the system to large strain deformations, the authors find a rejuvenation of the structure, which means a loss of aging, interpreted as a return of the system into the state before annealing.

The mentioned work gives hints at the possible changes of the glassy state by plastic deformations. Our intention is to elucidate for metallic glasses the effects of mechanical deformations on their structure and to consider also modifications in the atomic dynamics affecting, e.g., the relaxation processes.

In the following section II we present the basics of our simulation study, the characterization of our MD model, and a brief description of the applied methods. Section III reports the results of our simulations. Sections III A–III D cover in detail results from constant-strain-rate deformations, constant-shear-stress deformations at different stages of prestrained systems, fluctuation behavior of prestrained systems, and constant-shear-stress deformations of undeformed systems. Section IV completes the present work, including the discussion of our results and the conclusions.

II. SIMULATION

The MD simulations are carried out as isothermal simulations for a system of $N=5184$ particles in an orthorhombic simulation box with periodic boundary conditions. In our studies, the equations of motion of the N particles at temperature T are numerically integrated by a fifth-order predictor-corrector algorithm with time steps of typically 2×10^{-15} s. Temperature is introduced as the kinetic temperature determined from time averages of the kinetic energy (MD simulation details can be found in various textbooks—for example, Allen and Tildesley²³).

The interatomic couplings are modeled by short-ranged pair potentials, aimed at taking care of the electronic d -state interactions, and a volume-dependent s,p -state part as used in our previous studies (e.g., Teichler^{24,25}).

The deformations are carried out at two different temperatures below the computer model glass transition temperature, which is found to be $T_g \approx 1050$ K for the accessible cooling rates.⁸ Therefore configurations are prepared by cooling a 2000 K melt to 1020 K within nominally 270 ns (1.35×10^8 integration steps) and subsequently annealing it at this temperature for about 100 ns. After that the temperature is further decreased to 810 K with a cooling rate $\dot{T} = 10^{10}$ K/s. Configurations at $T=1000$ K and $T=810$ K are picked and annealed at the respective temperatures the next 10 ns and will be called parent configurations from now on. Similarly received configurations at different temperatures will be denoted depending on the particular temperature—for example, 1100 K-parent configuration, etc.

Deformations are imposed on these parent configurations using the Parrinello-Rahman scheme²⁶ where the simulation box extensions $L_{i,i=x,y,z}$ are introduced as new dynamical variables (the program uses the constraint of right angles for the simulation box). Two modes of deformation are analyzed: First, the forces (or stresses) acting on the faces of the simulation cell are defined. In order to attain these predefined forces a change of the L_i 's is allowed. This mode is used to simulate constant-shear-stress deformations. Second, the rate of change of the box dimensions \dot{L}_i can be set independently, resulting in a change of the systems stress state. The values can be taken in the way that the resulting shear strain rate is constant, whereas the strain in, e.g., the x direction at time t is defined as $[L_x(t) - L_x(0)]/L_x(0)$. This mode is used to model deformations at a constant strain rate. More detailed information about the simulation program used and the simulation techniques can be found in Refs. 27–29.

III. RESULTS

In the following we use the second invariants of the stress tensor $\boldsymbol{\sigma}$ and strain tensor $\boldsymbol{\epsilon}$ in order to introduce a coordinate-invariant measure of the shear deformations.³⁰ For example, the stress measure is given by

$$\sigma_M = \left\{ \frac{1}{2} \text{Tr}[(\boldsymbol{\sigma} - P \cdot \mathbf{1})^2] \right\}^{1/2}, \quad (1)$$

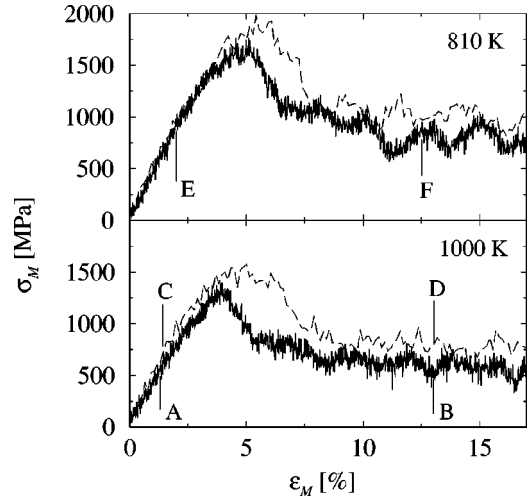


FIG. 1. Stress-strain curves for the deformation with a strain rate of 1.3%/ns (line) and 13.5%/ns (dashed line) at two temperatures. The lines denoted by A–F define different stages in the deformation history. Structures belonging to the stages A–F are investigated by further simulations (cf. Secs. III B and III C).

where $P = \frac{1}{3} \text{Tr}(\boldsymbol{\sigma})$ denotes the hydrostatic pressure. The strain measure ϵ_M is derived in the same way from $\boldsymbol{\epsilon}$.

A. Deformation under constant shear strain

Figure 1 shows the stress-strain curves for two different strain rates for deformations at the denoted temperatures. The shape of the stress-strain curves permits the definition of two distinct regimes: (i) The linear regime for strains up to 2%. In this regime the stress increases strongly and nearly linear with increasing strain. (ii) The flow regime for the strain value exceeding 7%. In this regime the stress value is drastically decreased compared to the maximum value at the yield point and is only slightly varying with increasing strain.

Regarding the shape of our simulated stress-strain curves it should be mentioned that its pronounced strain softening effect is well known for the deformation of polymeric glasses³¹ and it has been found to be a characteristic feature of some bulk metallic glasses strained at very high deformation rates.² There are also computer simulation studies like the MC simulations of Utz *et al.*,²² which yield similar results.

In Fig. 2 the development of the potential energy per atom, E_{pot} , is plotted for the stress-strain simulation runs shown in Fig. 1. After a quadratic increase at low strains, the energy turns to a linear strain dependence at large strains. The linear regime in the potential energy, Fig. 2, corresponds to the flow regime of the stress-strain curves, Fig. 1. Apparently, the weak dependence of E_{pot} on ϵ_M is a fingerprint of this flow state. The energy of the simulated flow state depends on the applied strain rate, with a higher strain rate leading to a higher value of E_{pot} .

The enhanced potential energy of the flow state obviously indicates a change of the structure of the simulated model. In order to measure this change, we use the Wendt-Abraham

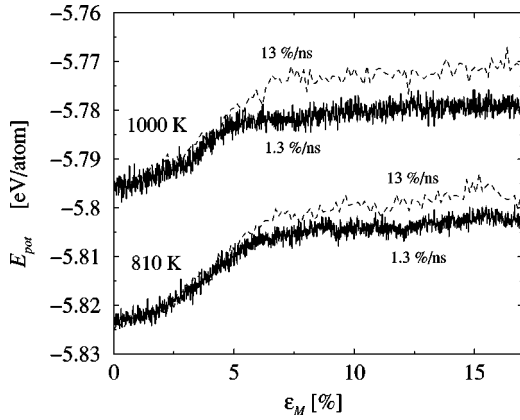


FIG. 2. Development of E_{pot} with strain for the deformations whose stress-strain curves are displayed in Fig. 1.

parameter³² R_{WA}^{Zr} in the Zr subsystem. R_{WA}^{Zr} is defined in terms of the radial distribution function $g_{ZrZr}(r)$ by the ratio of the $g_{ZrZr}(r)$ values at the first minimum and the first maximum. Table I shows the R_{WA}^{Zr} values for different strain regions of the stress-strain curves at different temperatures and strain rates. For evaluating R_{WA}^{Zr} , $g_{ZrZr}(r)$ is calculated by averaging over several configurations of the system belonging to the particular strain regions. Compared to the undeformed state, the flow state has an increased R_{WA}^{Zr} value, reflecting the change of structure.

Regarding the degree of modification of the system structure under the transition into the flow state at large plastic deformations, consider Fig. 3, showing the known linear temperature dependence of R_{WA}^{Zr} , with a change in slope at T_g . Included in the diagram are R_{WA}^{Zr} values for the 810 K- and 1000 K-parent configurations. Further, the diagram presents the R_{WA}^{Zr} value deduced for the flow state from the deformation with a strain rate of 13%/ns at 1000 K. The figure shows that the R_{WA}^{Zr} value in the flow state becomes comparable with that of an equilibrium system at a temperature which is about 200 K higher.

B. Deformation of prestrained configurations

For further characterizing the flow state, we have carried out constant-shear-stress deformations with predeformed configurations taken from the stress-strain-curve simulations at 1000 K. The considered configurations are indicated in Fig. 1 by the labels A–D. They are taken from the linear and flow regimes, respectively, and from 1.3%/ns and 13%/ns

TABLE I. R_{WA}^{Zr} deduced for different strain windows for the stress-strain curves of Fig. 1.

T [K]	$\dot{\epsilon}_M$ [%/ns]	R_{WA}^{Zr}		
		$\epsilon_M < 0.02$	$0.08 < \epsilon_M < 0.13$	$\epsilon_M > 0.14$
810	1.3	0.1437	0.1576	0.1572
810	13	0.1456	0.1637	0.1759
1000	1.3	0.1572	0.1675	0.1665
1000	13	0.1554	0.1793	0.1804

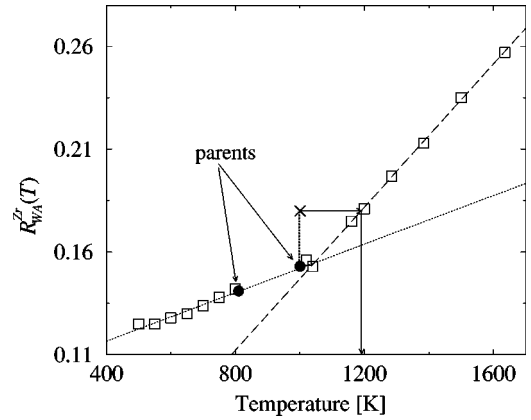


FIG. 3. Temperature dependence of R_{WA}^{Zr} (open squares). Indicated by arrows are the values for the parent configurations used for the deformation simulations (solid circles). Additionally plotted is the calculated Wendt-Abraham parameter for the flow regime of the stress-strain curve for $T = 1000$ K and $\dot{\epsilon}_M = 13\%/ns$ (cross).

strain rates. A pure shear with constant shear stress is imposed on these initial configurations, described through $-\sigma_{xx} = \sigma_{yy} = \sigma$ as the only nonzero values of the stress tensor (note that the value σ is only equal to our stress measure σ_M for this two-dimensional deformation mode).

Figure 4 displays the creep curves for configurations A–D, all of them subjected to the same shear stress of $\sigma_M = 664$ MPa.

It is obvious that the response of the system strongly depends on the regime of the stress-strain curves to which the configurations belong. A and C, from the linear regime, show no significant creep, whereas B and D (flow regime) are dramatically deformed. In terms of the shear viscosity, which can be calculated as the ratio of σ_M and the creep rate $\dot{\epsilon}_M$, the configurations from the flow state (B and D) are characterized by a viscosity being about four orders of magnitude smaller than that for the configurations from the linear regime (A and C).

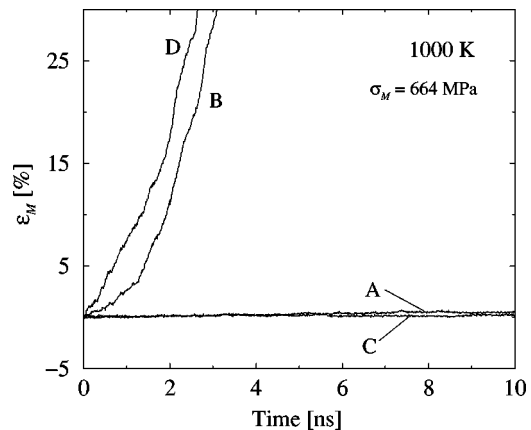


FIG. 4. Creep curves of four reference configurations (see text). The deformation simulations are carried out in the same way for configuration A–D. The configurations are only distinguished by the deformation history (cf. Fig. 1).

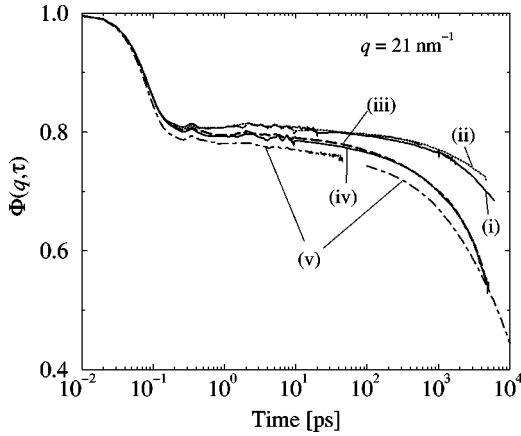


FIG. 5. Intermediate scattering function for the configurations defined in Table II.

C. Fluctuation dynamics of prestrained configurations

Here we provide results about changes of the fluctuation dynamics after straining the systems, visible, for example, in the intermediate scattering function. Regarding this, Fig. 5 presents the self-part of the intermediate scattering function $\Phi(q, \tau)$ deduced from 10-ns simulation runs starting with different initial configurations as given in Table II. The evaluation of $\Phi(q, \tau)$ is carried out for the last 5 ns of these runs with $q = 21 \text{ nm}^{-1}$, a q value that corresponds to the first maximum of the structure factor. The time window displayed in Fig. 5 covers the whole frequency range from thermal vibrations to the β - and α -decay regimes of density fluctuations as described by the mode coupling theory.^{33,34} The presented curves therefore display the fluctuation characteristics of a particular, history-dependent nonequilibrium state of the system.

Curves (i)–(iv) result from MD simulations at 1000 K using different initial configurations; curve (v) is simulated at 1100 K. The intermediate scattering functions (i)–(iv) coincide — more or less — in the initial vibrational decay regime below 0.2 ps. This reflects similar vibrational atomic motions

TABLE II. Characterization of the initial configurations for the 10-ns simulation runs used to calculate $\Phi(q, \tau)$. Configurations with numbers (i)–(v) are displayed in Fig. 5. For the deformed configurations A–F, cf. Fig. 1. The relaxation times τ_α are calculated (see text) for these simulation runs.

No	Initial configuration	Simulation temperature	τ_α
(i)	1000 K-parent	1000 K	92 ns
(ii)	deformed C	1000 K	165 ns
(iii)	deformed D	1000 K	31 ns
(iv)	1200 K-parent	1000 K	30 ns
(v)	1100 K-parent	1100 K	27 ns
-	deformed A	1000 K	189 ns
-	deformed B	1000 K	39 ns
-	810 K-parent	810 K	1190 ns
-	deformed E	810 K	≈ 3700 ns
-	deformed F	810 K	67 ns

in these cases. For curve (v) the vibrational decay is stronger due to the increased thermal motion. Accordingly, the short-time behavior below 0.2 ps seems to depend only on the simulation temperature with a more pronounced decay when the temperature is increased.

Regarding the α decay, let us first consider curves (i)–(iii). For the weakly prestrained curve (ii), Fig. 5 displays a delayed α decay compared to the undeformed parent structure (i). In contrast to this behavior, for the strongly prestrained configuration (iii), deformed up to the flow regime, the α decay takes place earlier than in the parent structure. Hence, the weakly prestrained configuration appears more rigid than the undeformed one and the strongly prestrained configuration displays a decreased viscosity. This is in agreement with the findings of Sec. III B.

In the β regime, which extends between the initial vibrational decay and the final α decay, the intermediate scattering function of the weakly prestrained structure (ii) exhibits no significant change compared to the parent structure (i). Different from this behavior, the structure (iii), taken from the flow state, shows a stronger β decay and falls below curves (i) and (ii). In the mode-coupling theory, the form of the intermediate scattering function in the β regime is ascribed to the “cage effect.” In this picture, the decrease of the intermediate scattering function in the β regime is suppressed because atoms are trapped in “cages” built by the surrounding atoms. The delayed breaking off of these cages leads to the late β and the α decays. Therefore, the modification in the β regime of curve (iii) indicates that the cages are broken off easier in the strongly predeformed structure than in the undeformed parent structure, again implying a loss of rigidity.

Let us now consider configurations (iv) and (v) and compare them with the configuration from the flow state, configuration (iii). Like curve (iii), curve (v) from the 1100 K-parent configuration shows a markedly lower α -decay time than (i) and (ii). But compared to curve (iii), the short-time vibrational decay for curve (v) is too strong. The features of the strongly prestrained configuration can be interpreted in more detail by introducing the concept of short-range order in the structure and its temperature dependence. Regarding this, we consider a simulated melt equilibrated at 1200 K and rapidly quenched to 1000 K. The system thus has the short-range order of the 1200 K melt, but the thermal fluctuations of a 1000 K structure. The intermediate scattering function of this structure is included in Fig. 5 as curve (iv). This curve shows the fluctuation decay expected at 1000 K but a faster α decay — a similar behavior as found for the strongly prestrained curve (iii). Therefore, taking the simulation temperature as a reference, the flow state behaves like a system having a fluctuation spectrum as expected for this temperature but a structure similar to that at a higher temperature.

To obtain a quantitative picture of the change in the α regime, the relaxation times τ_α are calculated (see Table II) from the adaptation of a stretched exponential function $\Phi^\alpha(q, \tau) \sim \exp[-(\tau/\tau_\alpha)^\beta]$ to the determined $\Phi(q, \tau)$ curves for long times³⁵ (adapted curves are not shown in Fig. 5 for clarity). These values indicate, as is visible in the $\Phi(q, \tau)$ curves in Fig. 5, an increasing relaxation time for weakly

strained systems and a decrease for initial configurations belonging to the flow regime. If the τ_α values are taken as a measure of the “age” of the simulated system, the fluctuation dynamics indicates deformation-dependent changes of the system age. Thus, the here-described modified fluctuation dynamics and the structural changes (see Sec. III A) can be interpreted in terms of the aging and rejuvenation effects reported for polymeric glasses.^{31,36}

The changes in the fluctuation dynamics for the system belonging to the flow state show the same features as recently described by Berthier, Barrat, and Kurchan³⁷ based on a theoretical model whose dynamics is given by a Langevin equation. Their model was subjected to a driving force having in mind the situation of a sheared fluid. The investigated correlation function³⁷ is comparable to that used in our work. They found for the driven steady state a so-called two-time-scale, two-temperature scenario: a typical two-step decay in the correlation function with the modification that only the primary decay is equal to an undriven system (caused by the “heat bath”). The secondary, final decay is faster due to the driving effects and could be described by an increased effective temperature. But note that Berthier *et al.*³⁷ observe the faster decay during the action of the driving force, while it is found in a load-free prestrained situation in our simulations. According to our results, the faster decay is due to a change of the viscosity of the system and not an effect of the driving force.

D. Deformation under constant shear stress

In this section we report results for the simulated $\text{Ni}_{0.5}\text{Zr}_{0.5}$ system subjected to deformations under constant shear stress. The parent configurations are exposed to a pure shear stress characterized by a stress tensor with $\sigma_{xx} = \sigma_{yy} = -2\sigma_{zz}$ and $\sigma_{ij} = 0$ if $i \neq j$.

In the following, we distinguish between deformation simulations restricted to strain values well below the yield point strain of $\epsilon_M \sim 5\%$ (cf. Fig. 1) and those reaching strains beyond this point. According to the constant-strain-rate simulations of Secs. III A–III C, in the first case the system remains close to the linear, elastic deformation regime where increased deformations induce structural changes, which lead to a more aged behavior. In the second case, the deformations reach strain values for which rejuvenation occurs under constant-strain-rate conditions, which means that a significant change of the structure takes place. Below, the results for the low-strain case are analyzed in terms of the conventional theory of thermally activated deformation processes^{18,19} intended to describe structural reorientations of small volume fractions inside an unchanged matrix. In the large-strain case, the deformations completely destroy the topology of the undeformed system and lead to a situation outside the applicability of these conventional models.

1. Deformations below 5% strain

The deformations are analyzed by use of the creep curves, which reveal the evolution of strain with time. The simulated deformation procedures are as follows: For the simulations at 1000 K a constant shear stress is applied for 10 ns. The stress

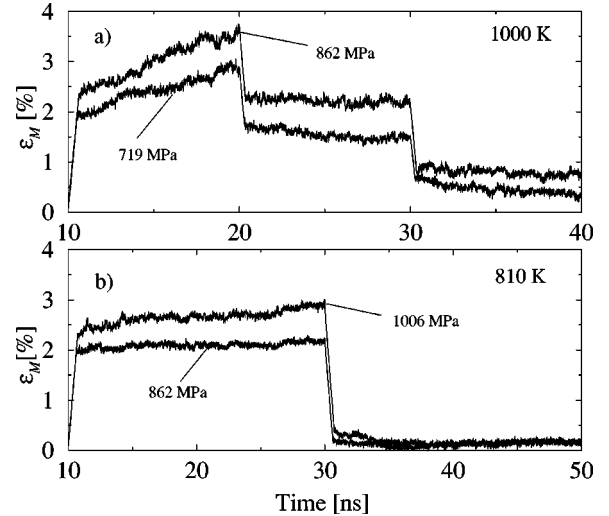


FIG. 6. (a) Strain evolution during deformation of our MD model for two different initial shear stresses at 1000 K. Halving is applied at $t = 20$ ns and unloading at $t = 30$ ns. (b) Strain evolution with time at 810 K. The load is removed at $t = 30$ ns.

then is reduced to half its value and the system is allowed to relax and deform under this lower stress value for an additional 10 ns. After that time, the applied stress is removed and the relaxation of the system is recorded for further 10 ns. At 810 K, a constant shear stress is applied for 20 ns and is removed after that time so that the system can relax for a further 20 ns without a load. Variable initial shear-stress values are used at both temperatures and the loading and unloading is done with a shear-stress rate $\dot{\sigma}_M = 1300$ MPa/ns for all simulations. As an example, Fig. 6 shows the strain evolution with time for different initial stress values at 1000 K and 810 K, respectively.

For the initial creep in Fig. 6 — before changing the load — one observes a nearly linear increase in the $\epsilon_M(t)$ curves, implying a steady-state viscoelastic-anelastic creep. The load reductions after 20 ns for the 1000 K case and the unloading after 30 ns for both temperatures are accompanied by subsequent strain drops, reflecting the elastic parts of the strain. After the strain drops, the system shows strain relaxation phenomena, resulting in slight decreases in the $\epsilon_M(t)$ curves. Such an anelastic recovery effect is well known for the low-load deformations of metallic glasses and was investigated experimentally, for example, by Weiss *et al.*⁶ who interpreted their results in terms of the earlier model of Tsao and Spaepen.⁴³ At least for the 1000 K simulations, Fig. 6(a), our creep curves show that the recovery seems to be more pronounced for the weaker-deformed system. This is in agreement with the discussion by Argon and Shi⁴⁴ on the transition from an anelastic to plastic response in amorphous systems under increasing deformation. According to these authors, plastic deformation evolves at larger strains, because the overall fraction of transformed regions increases, raising the possibility of finding closely neighbored deformed zones, which results in a loss of memory in the surroundings of a particular deformed region. After reducing the load during the 1000 K simulations, no strain increase is observed between 20 and 30 ns. This may be an indication that in the

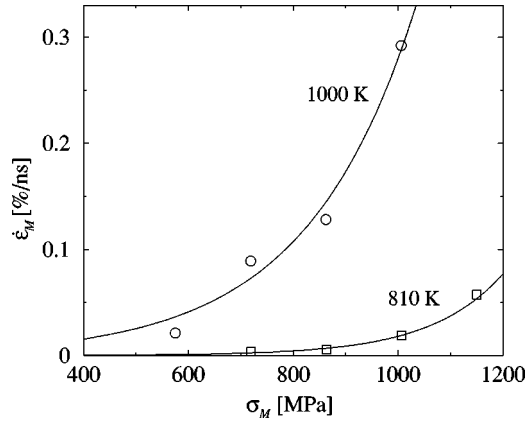


FIG. 7. Strain rate vs shear-stress dependence evaluated from the MD-simulated deformation of our $\text{Ni}_{0.5}\text{Zr}_{0.5}$ model at two different temperatures.

considered time window anelastic recovery dominates the dynamics. For both temperatures the final plastic deformation is less than 1%, while deformations at the higher temperature result in larger final strains.

Figure 7 displays the strain rates deduced from deformations at various initial stress values for the two temperatures. The strain rates are calculated using a linear regression analysis of $\epsilon_M(t)$ in the time windows between 11 and 19 ns at 1000 K (11–17 ns for the largest stress value at 1000 K; see below) and 11–29 ns at 810 K. Figure 7 indicates a non-Newtonian creep behavior which is a key characteristic for the homogeneous flow in metallic glasses.^{3,18,19,4} We use the well-established hyperbolic sine law^{18,19} $\dot{\epsilon}_M \sim \sinh[\Omega\sigma_M/kT]$ to analyze the shear-strain rate versus shear-stress dependence at a given temperature. This leads to an activation volume of the order $\Omega \approx 7-8 \times 10^{-29} \text{ m}^3$. This is close to the values of experimentally determined activation volumes^{4,38,39} and also similar to that reported for a MD-simulated Lennard-Jones system by Tomida and Egami.²⁰

2. Deformations above 5% strain

Figure 8(a) displays the creep curve at $T=1000 \text{ K}$ resulting from a simulated deformation with an initial stress of $\sigma_M=1006 \text{ MPa}$. It exhibits an instability under constant shear stress: The MD model shows a deformation with nearly linear increasing strain as expected. Then, after about $t=17 \text{ ns}$, an increasing strain rate can be observed, leading to a dramatic shearing of the model. At $t=20 \text{ ns}$, when reducing the loading stress to half its value, the increase stops. During the following 10 ns of deformation with the reduced load, the system seems to establish another steady-state creep where the strain rate decreases again to a smaller value. After unloading at $t=30 \text{ ns}$, the final plastic deformation is about 60%.

Figure 8(b) represents the R_{WA}^{Zr} values which result from an evaluation of the radial distribution functions for different time windows of the MD data from the simulated creep-curve displayed in Fig. 8(a). If a specific time window has initial and final times t_i and t_f , respectively, then the R_{WA}^{Zr} value for that particular time window is plotted at time t

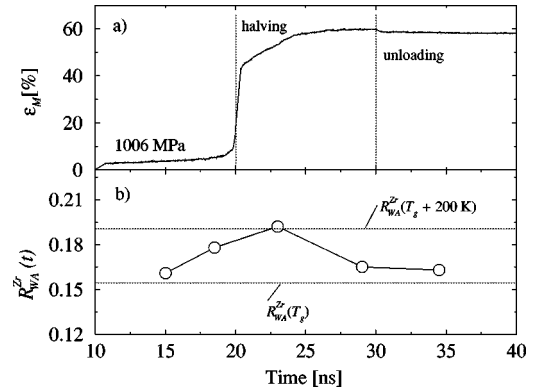


FIG. 8. (a) Evolution of strain with time during creep at $T = 1000 \text{ K}$ and an initial stress of $\sigma_M = 1006 \text{ MPa}$. The dotted lines indicate the simulation times at which changing of the imposed load occurs. (b) Evaluated R_{WA}^{Zr} -values at different times for the creep curve from (a) (see text).

$= 0.5(t_f - t_i)$. As guides to the eye the R_{WA}^{Zr} values for $T = T_g$ and $T = T_g + 200 \text{ K}$ are contained in Fig. 8(b) indicated by lines. During the instability a strong increase of the R_{WA}^{Zr} value is observed whereas after unloading R_{WA}^{Zr} decreases again, reaching nearly the starting value.

Accordingly, the instability seems to be caused by a structural change in the system. Comparison of these findings with those from the constant-strain-rate deformations of Sec. III A reveals that the instability is analogous to the transition into the flow state. Thus, application of large enough stresses leads to a change of the system state towards one which easily is able to maintain the large strain rates.

IV. DISCUSSION

First let us summarize the basic results presented so far in the paper.

(1) Simulated plastic deformation under a constant high strain rate leads to stress-strain curves resembling the experimental ones (see especially Kato *et al.*²). The stress overshoot and the subsequent strain softening effect reflect a transition from a hardly deformable state into a flow state, which carries the plastic deformation easily. Depending on the strain rate, the potential energy of the flow state is altered to higher values, which imply a change of structure in the MD model towards a more liquid one.

(2) Shearing with a constant shear-strain rate results in aging or rejuvenation of the structure, depending on the degree of deformation. As can be seen from the α -relaxation times of prestrained samples, weakly prestrained ones show a larger relaxation time than the unstrained samples. That means there is an aging effect under these conditions. Aging is observed as long as the system remains in the linear regime during prestraining. In the case of large prestraining, after the transition into the flow state, the samples exhibit a decreased α -relaxation time compared to the unstrained ones, which means they show the feature of rejuvenation.

(3) Deformation under constant shear stress σ_M leads to a linear increase in strain, which means a constant strain rate

$\dot{\epsilon}_M$, at least for the here studied deformations of less than 5% total strain. The stress dependence of $\dot{\epsilon}_M$ can be well described by the sinh law,^{18,19} yielding an activation volume of $7-8 \times 10^{-29} \text{ m}^3$ which nearly equals 5 times the atomic volume.

(4) In the particular case of a high, constant shear stress, well above the flow stress value, an instability was observed after about 5% deformation: a dramatic reduction of the viscosity of the system takes place, leading to a catastrophic increase of the strain rate (compare Fig. 8, Sec. III D). From the deformation dependence of the Wendt-Abraham parameter, R_{WA}^{Zr} , this instability under constant shear stress has been identified as the transition into the flow state.

We note that values like R_{WA}^{Zr} or the relaxation time τ_α are isotropic diagnostic means aimed at characterizing the gross features of the structural changes induced by high-strain-rate deformations. One should be aware that mechanical deformations induce, in addition, an anisotropy of the system as analyzed, e.g., by Tomida and Egami.²⁰

A. Deformation with large strain rates

As a consequence of high-strain-rate deformations, our simulations clearly show a change of state of the system towards a more easily deformable one: the flow state. It is characterized by an obvious increase in the potential energy and a change of the structure towards a more disordered one indicated by the change of R_{WA}^{Zr} and has to be viewed as a driven, stationary state, differing from that of the respective parent configuration. The latter can be concluded from the instability and its stopping under load reduction, Fig 8: When the catastrophic straining is stopped by reducing the load, the structure of the model, as far as reflected by the Wendt-Abraham parameter, relaxes back towards that at the beginning of the creep deformation.

The increase of the energy and the enhanced structural disordering in the flow state depend mainly on the strain rate and only weakly on the simulation temperature. The gap between the potential energy curves at different temperatures visible in Fig. 2, Sec. III A, is due to vibrational displacements of the atoms. According to the virial theorem for harmonic excitations, the mean potential energy E_{pot} stored in the vibrational displacements is equal to the mean kinetic energy per atom, E_{kin} . Therefore, the configurational part of the potential energy can be estimated by considering $E_{pot} - E_{kin}$, which means elimination of the vibrational contributions. In Fig. 9, $E_{pot} - E_{kin}$ is plotted against the strain for the deformation simulations with a strain rate of 1.3%/ns. The data indicate an independence of the configurational part of the potential energy, $E_{pot} - E_{kin}$, from the initial temperature for the flow-state regime.

Regarding the structural changes during the transition into the flow state, it is noteworthy to refer to the work of Polk and Turnbull.⁴⁰ There the authors speculate on how the structure of a glassy system is affected by a deformation at a given strain rate or stress, when the latter is above some characteristic limit.⁴⁰ They explain that during deformation at high rates a nonequilibrium structure should be present which differs from the one in equilibrium in a way that it is

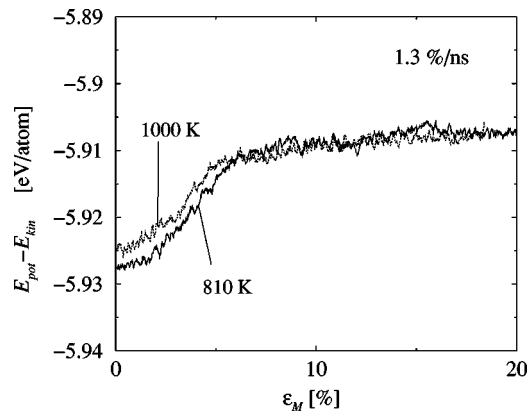


FIG. 9. Evolution of $E_{pot} - E_{kin}$ with strain for the MD-simulated deformation of our $\text{Ni}_{0.5}\text{Zr}_{0.5}$ model at two different temperatures for a strain rate of 1.3%/ns. The curves were lightly smoothed to get a clearer distinction between the energies of the parent configurations ($\epsilon_M=0$).

more “disordered.” They also make suggestions on the manner in which the enhanced disorder could occur: due to (i) a “greater compositional disordering” or (ii) an increase in the “average atomic volume.” It is also argued⁴⁰ that this non-equilibrium structure is comparable to an equilibrium structure at higher temperatures “without an actual temperature increase.”

Our simulation study is in agreement with these assumptions. For our model amorphous metal, the enhanced structural disorder arises from an increase in compositional disorder. A change of the average atomic volume can be excluded because the volume in our constant-strain-rate simulations is kept constant. The Wendt-Abraham parameter can be used as a simple measure of the effective structural temperature increase (cf. Sec. III A).

We further note that evidence is found also in experiments for the here-described transition into the flow state—for example, in those by Popescu⁴¹ on tensile deformation tests of $\text{Fe}_{80}\text{B}_{20}$ metallic glass or by Koba *et al.*⁴² on the rolling and bending of $\text{Fe}_{40}\text{Ni}_{38}\text{Mo}_4\text{B}_{18}$ and $\text{Co}_{56}\text{Ni}_{10}\text{Fe}_5\text{Si}_{12}\text{B}_{17}$ metallic glasses. Comparing the x-ray diffraction patterns of as-quenched and deformed samples, they found a decreasing intensity for the first and second diffraction peaks for the deformed specimen, which they use as an indication of increased structural disorder. Popescu⁴¹ refers to the work of Polk and Turnbull⁴⁰ and gives arguments that his observations are due to an increased compositional disorder, although volume conservation is not maintained in his experiments.

B. Aging and rejuvenation during shear deformation

Analysis of the structural fluctuations in our MD model in terms of the self-part of the intermediate scattering function $\Phi(q, \tau)$ reveals the effects of aging and rejuvenation, depending on whether the reached strain is small or large. Rejuvenation of a Lennard-Jones glass has been reported by Utz *et al.*²² from MC simulations of shearing. There, rejuvenation is characterized through a change of the radial distribution function and an increase in potential energy.

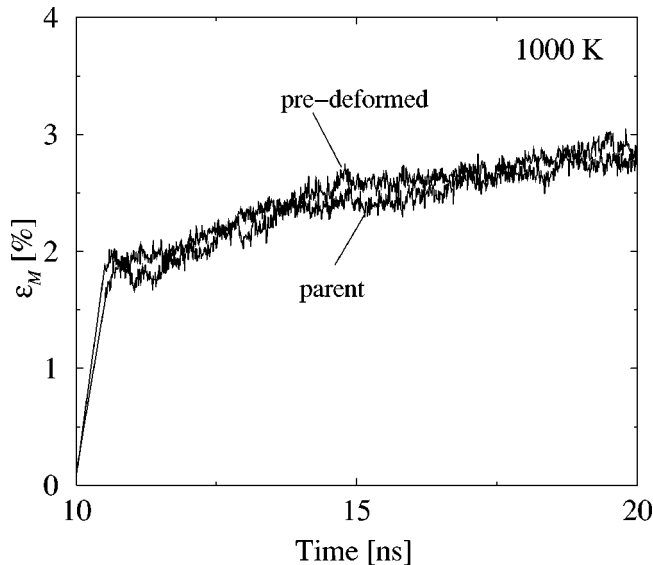


FIG. 10. Simulated creep curves with $\sigma_M = 719$ MPa at 1000 K for two different initial configurations. The parent curve is identical to that in Fig. 6(a). The curve “predeformed” starts from the simulation run of the parent configuration after a deformation at $\sigma_M = 719$ MPa for a time of nearly 10 ns. Obviously these two creep curves describe a similar response of the MD model against loading. That means a significant change in the structure has not occurred during predeformation.

Our MD simulations demonstrate that rejuvenation also involves modifications of the fluctuation dynamics of the system, in addition to the structural changes (see Sec. III C). The modifications of the dynamics are visible in the position and heights of the α relaxation peak. They imply a change of the fluctuation behavior in the β -regime, while the thermal vibrations are not affected by rejuvenation but reflect the simulation temperature.

Apart from that, our simulations exhibit a phenomenon which is reported, to our knowledge, for the first time: an increase in the α -relaxation time of weakly sheared systems, indicating additional aging of the model amorphous structure (and offering the possibility of generating more rigid amorphous structures by weakly shearing them).

These findings can be explained in the energy landscape picture^{45–47} as an effect of exploration of the high-dimensional potential energy hypersurface by the system. By weakly straining, the system is driven rapidly through the configuration space until regions of increased potential barriers are reached, resulting in the reported increased rigidity (Sec. III B) or the increase in α -relaxation times (Sec. III C). If the deformation proceeds, the system surmounts those higher-energy barriers after a certain time and is driven into regions of the potential energy hypersurface normally belonging to an equilibrium melt, resulting in the rejuvenation effect as determined, for example, by the decreased relaxation times (Sec. III C). Details of possible mechanisms allowing the exploration of the energy landscape can be found for example in Ref. 48.

C. Homogeneous and heterogeneous deformations in metallic glasses

From experiments it is known that the deformation in metallic glasses depends on temperature and imposed load, allowing two different modes of deformation:⁴⁹ homogeneous deformation at high temperatures and low loads and heterogeneous deformation at low temperatures and high loads. The latter mode leads to the formation of shear bands appearing as localized highly deformed regions in the sample. These properties are often summarized in so called deformation maps as, for example, presented by Spaepen for Pd-based metallic glasses.¹⁸

Although our simulations are carried out at temperatures close to the homogeneous deformation regime,⁴⁹ two distinct modes of deformation are observed. It well may be that these modes can be related to the structural dynamics in the experimentally found homogeneous and heterogeneous deformations.

The first mode, observed in the simulations, is present in the constant-shear-stress deformations of Sec. III D and leads to moderate strain rates (the curve with the instability should be excluded here). In this mode, the deformation is not accompanied by a drastic change of the state of the system as can be seen in Fig. 10, where a predeformed system is sheared again, resembling a more or less unchanged creep curve compared to the first one (details in Fig. 10). The second mode appears as the transition into the flow state for deformations at high strain rates (see Sec. III A), changing the state of the system in the above-described manner (higher potential energy, etc.).

Experiments indicate structural changes in shear bands which are often explained by an increased disorder. This is concluded, for example, from observations of a modified etching behavior of surfaces in regions where shear bands occur^{50,51} or from variations in the microhardness,⁴² with decreasing microhardness if the measurements were performed in regions of increased shear band density, implying a loss of rigidity in those regions. Note that the flow state is characterized through an increased disorder, taking R_{WA}^{Zr} as a measure (Sec. III A) and a lowered rigidity (Sec. III B).

Therefrom it is tempting to assume that our first mode models the structural dynamics during homogeneous deformation and the second mode characterizes the dynamics in the interior of a shear band during heterogeneous deformation. In this picture, the occurrence of shear bands reflects a transition into this second mode for a confined, platelike part of the volume.

ACKNOWLEDGMENTS

The authors acknowledge support by the Research Center Jülich and the RRZN Hannover by providing computer capacities and computer time for carrying out the simulations.

- *Electronic address: kbrinkm@ump.gwdg.de
- ¹Y. Kawamura, T. Shibata, A. Inoue, and T. Masumoto, *Appl. Phys. Lett.* **69**, 1208 (1996).
 - ²H. Kato, Y. Kawamura, A. Inoue, and H. S. Chen, *Appl. Phys. Lett.* **73**, 3665 (1998).
 - ³R. Maddin and T. Masumoto, *Mater. Sci. Eng.* **9**, 153 (1972).
 - ⁴A. I. Taub, *Acta Metall.* **28**, 633 (1980).
 - ⁵J. Stromböm, P. J. Henderson, and S. J. Savage, *Scr. Metall. Mater.* **27**, 1179 (1992).
 - ⁶M. Weiss, M. Moske, and K. Samwer, *Appl. Phys. Lett.* **69**, 3200 (1996).
 - ⁷V. Ocelik, Y. V. Fursova, V. A. Khonik, and K. Csach, *Phys. Solid State* **42**, 697 (2000).
 - ⁸H. Teichler, *Phys. Rev. B* **59**, 8473 (1999).
 - ⁹H. Teichler, *Defect Diffus. Forum* **143-147**, 717 (1997).
 - ¹⁰Z. Altounian, Guo-Hua Tu, and J. O. Strom-Ohlsen, *J. Appl. Phys.* **54**, 3111 (1983).
 - ¹¹J. Eckert, L. Schultz, and K. Urban, *J. Mater. Res.* **6**, 1874 (1991).
 - ¹²J. R. Gachon, M. Dirand, and J. Hertz, *J. Less-Common Met.* **92**, 307 (1983).
 - ¹³F. Gärtner, Ph.D. thesis, University of Göttingen, 1992.
 - ¹⁴A. Inoue, T. Zhang, and T. Masumoto, *Mater. Trans., JIM* **31**, 425 (1990); A. Inoue, T. Nakamura, N. Nishiyama, and T. Masumoto, *ibid.* **33**, 937 (1992).
 - ¹⁵F. Mezei, W. Knaak, and B. Farago, *Phys. Rev. Lett.* **58**, 571 (1987).
 - ¹⁶U. Krieger and J. Bosse, *Phys. Rev. Lett.* **59**, 1601 (1987).
 - ¹⁷D. Richter, B. Frick, and B. Farago, *Phys. Rev. Lett.* **61**, 2465 (1988).
 - ¹⁸F. Spaepen, *Acta Metall.* **25**, 407 (1977).
 - ¹⁹A. S. Argon, *Acta Metall.* **27**, 47 (1979).
 - ²⁰T. Tomida and T. Egami, *Phys. Rev. B* **48**, 3048 (1993).
 - ²¹M. L. Falk and J. S. Langer, *Phys. Rev. E* **57**, 7192 (1998).
 - ²²M. Utz, P. G. Debenedetti, and F. H. Stillinger, *Phys. Rev. Lett.* **84**, 1471 (2000).
 - ²³M. P. Allen and D. J. Tildesley, *Computer Simulation of Liquids* (Clarendon, Oxford, 1987).
 - ²⁴H. Teichler, *Phys. Status Solidi B* **172**, 325 (1992).
 - ²⁵H. Teichler, *Phys. Rev. Lett.* **76**, 62 (1996).
 - ²⁶M. Parrinello and A. Rahman, *J. Appl. Phys.* **52**, 7182 (1981).
 - ²⁷T. Aspelmeyer, diploma thesis, University of Göttingen, 1995.
 - ²⁸B. Böttdeker and H. Teichler, *Phys. Rev. E* **59**, 1948 (1999).
 - ²⁹B. Böttdeker and H. Teichler, in *Molecular Dynamics on Parallel Computers*, edited by R. Esser, P. Grassberger, J. Grotendorst, and M. Lewrenz (World Scientific, Singapore, 2000).
 - ³⁰V. V. Sokolovskij, *Theorie der Plastizität* (VEB Verlag Technik, Berlin, 1955).
 - ³¹A. S. Argon, in *Plastic Deformation and Fracture of Materials*, Materials Science and Technology Vol. 6, edited by R. W. Cahn, P. Haasen, and E. J. Kramer (VCH, Weinheim, 1993), Chap. 10.
 - ³²H. R. Wendt and F. F. Abraham, *Phys. Rev. Lett.* **41**, 1244 (1978).
 - ³³W. Götze and L. Sjögren, *J. Phys. C* **21**, 3407 (1988).
 - ³⁴L. Sjögren, *Z. Phys. B: Condens. Matter* **79**, 5 (1990).
 - ³⁵W. Götze and L. Sjögren, *Rep. Prog. Phys.* **55**, 241 (1992).
 - ³⁶M. M. Santore, R. S. Duran, and G. B. McKenna, *Polymer* **31**, 2377 (1991).
 - ³⁷L. Berthier, J.-L. Barrat, and J. Kurchan, *Phys. Rev. E* **61**, 5464 (2000).
 - ³⁸A. I. Taub, *Scr. Metall.* **17**, 873 (1983).
 - ³⁹H. Höfler, R. S. Averbach, G. Rummel, and H. Mehrer, *Philos. Mag. Lett.* **66**, 301 (1992).
 - ⁴⁰D. E. Polk and D. Turnbull, *Acta Metall.* **20**, 493 (1972).
 - ⁴¹M. A. Popescu, *J. Non-Cryst. Solids* **169**, 155 (1994).
 - ⁴²E. S. Koba, Yu. V. Milman, and A. P. Rachek, *Acta Metall. Mater.* **42**, 1383 (1994).
 - ⁴³S. S. Tsao and F. Spaepen, *Acta Metall.* **33**, 891 (1985).
 - ⁴⁴A. S. Argon and L. T. Shi, *Acta Metall.* **31**, 499 (1983).
 - ⁴⁵F. H. Stillinger and T. A. Weber, *Phys. Rev. A* **28**, 2408 (1983).
 - ⁴⁶C. A. Angell, *J. Non-Cryst. Solids* **131-133**, 13 (1991).
 - ⁴⁷F. H. Stillinger, *Science* **267**, 1935 (1995).
 - ⁴⁸D. L. Malandro and D. J. Lacks, *J. Chem. Phys.* **110**, 4593 (1999).
 - ⁴⁹D. Srolovitz, V. Vitek, and T. Egami, *Acta Metall.* **31**, 335 (1983).
 - ⁵⁰C. A. Pampillo, *Scr. Metall.* **6**, 915 (1972).
 - ⁵¹C. A. Pampillo and H. S. Chen, *Mater. Sci. Eng.* **13**, 181 (1974).